Journal of Solid State Chemistry 230 (2015) 279–286

Contents lists available at ScienceDirect

Journal of Solid State Chemistry

journal homepage: www.elsevier.com/locate/jssc

Structure, stability, and photoluminescence in the anti-perovskites $Na_3W_{1-x}Mo_xO_4F$ $(0 \leq x \leq 1)$

Eirin Sullivan [a,*], Maxim Avdeev [b], Douglas A. Blom [d], Casey J. Gahrs [a], Robert L. Green [c,d], Christopher G. Hamaker [a], Thomas Vogt [b,d]

[a] Department of Chemistry, Illinois State University, Normal, IL 61790, USA
[b] Bragg Institute, Australian Science and Technology Organization, Locked Bag 2001, Kirrawee DC, NSW 2234, Australia
[c] Department of Chemistry, Allen University, Columbia, SC 29204, USA
[d] Nanocenter and Department of Chemistry and Biochemistry, University of South Carolina, Columbia, SC 29208, USA

ARTICLE INFO

Article history:
Received 18 March 2015
Received in revised form
10 July 2015
Accepted 13 July 2015
Available online 14 July 2015

Keywords:
Oxyfluorides
Neutron powder diffraction
Powder X-ray diffraction
Single crystal X-ray diffraction
Optical properties

ABSTRACT

Single-phase ordered oxyfluorides Na_3WO_4F, Na_3MoO_4F and their mixed members $Na_3W_{1-x}Mo_xO_4F$ can be prepared *via* facile solid state reaction of $Na_2MO_4 \cdot 2H_2O$ (M=W, Mo) and NaF. Phases produced from incongruent melts are metastable, but lower temperatures allow for a facile one-step synthesis. In polycrystalline samples of $Na_3W_{1-x}Mo_xO_4F$, the presence of Mo stabilizes the structure against decomposition to spinel phases. Photoluminescence studies show that upon excitation with λ=254 nm and λ=365 nm, Na_3WO_4F and Na_3MoO_4F exhibit broad emission maxima centered around 485 nm. These materials constitute new members of the family of self-activating ordered oxyfluoride phosphors with anti-perovskite structures which are amenable to doping with emitters such as Eu^{3+}.

1. Introduction

Tungstates, in particular scheelite ($CaWO_4$), are suitable for many applications. They are used as phosphor host lattice materials due to their intrinsic self-activating photoluminescence arising from electron transfer within the WO_4^{2-} ions (or WO_6^{6-} ions in wolframite-type phases). Additionally, as tungsten possesses a high atomic number (Z), high-density tungsten-containing single crystals are widely used as scintillation detectors for high-energy radiation and particles.

Tungsten compounds with the general formula AWO_4 have been shown to exhibit either the scheelite or wolframite structure. Smaller A cations (ionic radius <1 Å) favor the monoclinic wolframite structure (A=Mg, Mn, Fe, Co, Ni, Zn, Cd) [1] whilst larger M cations (ionic radius >1 Å) adopt the tetragonal scheelite structure (A=Ca, Sr, Ba, Pb, Eu) [2].

Upon excitation with λ=240 nm, $CaWO_4$ exhibits a blue broadband photoluminescence centered near 440 nm, whilst excitation with λ=315 nm shifts this broad emission to 520 nm (green region) accompanied by two zero-phonon lines at 368 nm and 375 nm [3]. Nazarov et al. co-doped $CaWO_4$ with Eu^{3+} and Tb^{3+} and showed that the dominant line emissions for Eu^{3+} at 619 nm (red; $^5D_0 \rightarrow {}^7F_2$) and Tb^{3+} at 543 nm (green: $^5D_4 \rightarrow {}^7F_5$) combined with excitation of the host lattice at λ=147 nm to produce white light [4]. The photoluminescent behavior of the Mo-analog, $CaMoO_4$, is similar to that of $CaWO_4$, with the broad band shifted into the green region [5,6]. Broad-band photoluminescence peaks in the region between 480 and 490 nm have also been observed in the wolframite family of tungstates, such as $ZnWO_4$ which exhibits a broad-band centered at 480 nm [7,8].

The tungsten and molybdenum-containing scheelite solid solution $NaM(WO_4)_{2-x}(MoO_4)_x{:}Eu^{3+}$ (M=Gd, Y, Bi) demonstrates how fine tuning the tungsten and molybdenum content can be used to optimize the absorption range for new phosphors in $In_{1-x}Ga_xN$ LEDs. Current fluorescent phosphors are optimized for mercury discharge lamps which primarily emit light at 254 nm and 365 nm. Phosphors for use in phosphor-conversion LEDs (PC-LEDs) should have excitations in the near-UV range to efficiently absorb light emissions from $In_{1-x}Ga_xN$, approximately ranging from 370 nm (x=0) to 440 nm (x=0.3). The emission spectra of $NaY(WO_4)_{2-x}(MoO_4)_x{:}Eu^{3+}$ showed line emissions at λ=591 nm, 615 nm, 654 nm, and 701 nm corresponding to $^5D_0 \rightarrow {}^7F_J$ (J=1, 2, 3, 4). With increasing Mo concentration, additional lines appeared at λ=577 nm ($^5D_1 \rightarrow {}^7F_0$) and 584 nm ($^5D_1 \rightarrow {}^7F_3$) and the $^5D_0 \rightarrow {}^7F_J$ lines broadened. In addition to sharp lines corresponding to Eu^{3+} transitions, the excitation spectra showed a broad absorption centered near $\approx$300 nm attributed to O→W/Mo charge transfer.

* Corresponding author.
E-mail address: esulliv@ilstu.edu (E. Sullivan).

http://dx.doi.org/10.1016/j.jssc.2015.07.018
0022-4596/

Importantly, increasing the Mo content shifted this charge transfer band towards 350 nm which is approaching the near-UV range required for $In_{1-x}Ga_xN$ LEDs [9].

Recently there has been a surge in interest in crystalline oxyfluoride phosphors due to their suitability for use in phosphor-conversion light emitting diode (PC-LED) devices [10]. Tungsten or molybdenum oxyfluorides are candidates which might display new photoluminescent and/or scintillator properties for high energy radiation. Photoluminescence has been reported for the crystalline tungsten oxyfluoride $Ba_2WO_3F_4$ (space group $C2/c$; lattice parameters $a=11.514$ Å, $b=9.383$ Å, $c=7.193$ Å, $\beta=126.17°$; *N.B.* no standard deviations reported [11,12]) wherein $Ba_2WO_3F_4$ was shown to emit blue-green light upon excitation with UV and X-rays. The excitation–emission spectrum for $Ba_2WO_3F_4$ shows a broad emission band centered at $\lambda=485$ nm upon excitation with $\lambda_{ex}=260$ nm, which shifts to a higher wavelength emission ($\lambda=505$ nm) when excited in the near-UV range ($\lambda_{ex}=305$ nm) [13]. An isostructural molybdenum phase, $Ba_2MoO_3F_4$, also shows photoluminescence, but due to the higher thermal quenching associated with the size of the Mo^{6+} cation as compared to W^{6+}, this analog only luminesces at low temperatures [14]. The emission spectra observed for $Ba_2WO_3F_4$ is very similar to wolframite $MgWO_4$, which has a broad emission band peaking around $\lambda=490$ nm [15]. The similarity in photoluminescent behavior between $Ba_2WO_3F_4$ and $MgWO_4$ is contrasted by the structural arrangements in the two materials: $Ba_2WO_3F_4$ contains linear chains of WO_4F_2 octahedra which are corner-linked *via* O^{2-} anions whilst wolframite $MgWO_4$ is comprised of zigzag chains of edge-sharing WO_6 octahedra.

Na_3WO_4F and the isostructural molybdenum analog were first found by Schmitz-Dumont and Weeg [16]. A detailed structural characterization of single crystals of Na_3WO_4F formed as the primary product of the reaction of $Na_2WO_4\cdot 2H_2O$ and YF_3 [17] (with the intention of synthesizing $YFWO_4$) showed that this material is isostructural with the anti-perovskites $NaCa_2SiO_4F$ [18] and $NaCa_2GeO_4F$ [19].

The anion-ordered sodium tungsten oxy-fluoride Na_3WO_4F (space group *Pnma*; lattice parameters $a=5.5959(8)$ Å, $b=7.5102(7)$ Å, $c=12.8598(9)$ Å [17]) is an anti-perovskite related structure which shows promise as a phosphor host lattice. In this material, Na^+ cations are distributed across two distinct sites and coordinated by four O^{2-} anions and two F^- anions resulting in a distorted octahedral coordination. These NaO_4F_2 octahedra form edge-sharing chains along *a*, which are in turn linked by vertex-sharing O^{2-} of the isolated WO_4 tetrahedra. The F^- anion has an octahedral FNa_6 coordination and forms face-sharing chains along the *a* direction. The Na_3WO_4F structure can be described as a hexagonal anti-perovskite where the WO_4 tetrahedra occupy the 12-coordinate A site and F^- is located on the B site and is octahedrally coordinated by the Na cations (Fig. 1).

The photoluminescent properties of Na_3WO_4F and Na_3MoO_4F have not been previously reported, although several materials which are known to be promising host lattices for use in PC-LED devices are oxyfluorides and crystallize in anti-perovskite structures [10], such as $Sr_{3-x}A_xMO_4F$ (A=Ca, Ba and M=Al, Ga) [20] and Sr_2LiSiO_4F [21,22].

2. Experimental

We investigated if single-phase samples of Na_3MO_4F (M=Mo, W) could be simply made by reaction of $Na_2MO_4\cdot 2H_2O$ (M=Mo, W) with NaF in a 1:1 stoichiometric ratio. Initially, Na_3WO_4F was prepared from appropriate quantities of $Na_2WO_4\cdot 2H_2O$ and NaF by heating for 8 h in air at 800 °C, producing an incongruent melt. A slow ramp rate of approximately 1 °C min^{-1} was used to ensure that the water present in $Na_2WO_4\cdot 2H_2O$ was not lost in a violent fashion. Similarly, Na_3MoO_4F was synthesized under the same conditions from $Na_2MoO_4\cdot H_2O$ and NaF. The mixed W/Mo series $Na_3W_{1-x}Mo_xO_4F$ ($x=0$, 0.25, 0.5, 0.75, 1) was prepared from the reaction of appropriate stoichiometric amounts of $Na_2WO_4\cdot 2H_2O$, $Na_2MoO_4\cdot H_2O$, and NaF. These conditions yielded the target products, but upon grinding and exposure to air, were observed to decompose to form mixtures of $Na_3W_{1-x}Mo_xO_4F$, Na_2WO_4/Na_2MoO_4, and NaF. The Eu^{3+}-containing samples $Na_{2.85}Eu_{0.05}MoO_4F$ and $Na_{2.85}Eu_{0.05}WO_4F$ were prepared using $Na_2WO_4\cdot 2H_2O$, $Na_2MoO_4\cdot H_2O$, NaF, and Eu_2O_3.

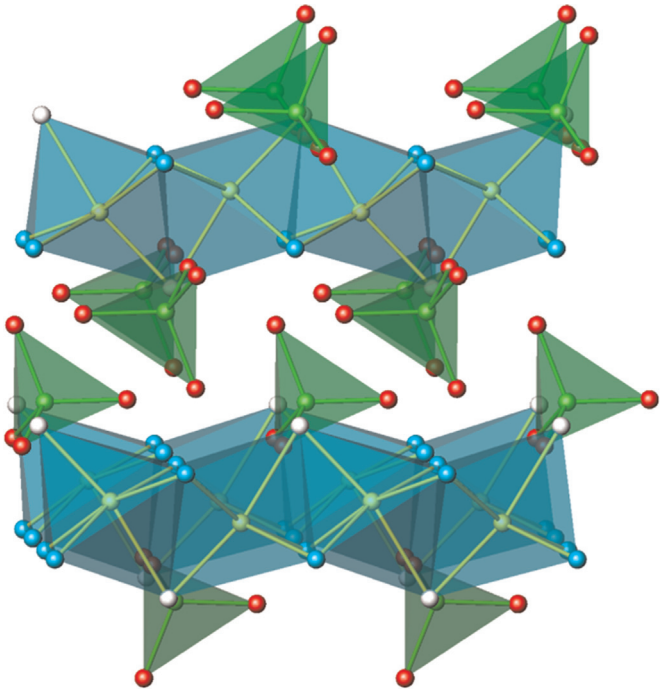

Fig. 1. The structure of Na_3WO_4F viewed in the ac-plane to show face-sharing FNa_6 octahedra and highlight the hexagonal anti-perovskite structure. The atom colors are as follows: Na(1) white, Na(2) cyan, W green, O red, and F yellow. (For interpretation of the references to color in this figure legend, the reader is referred to the web version of this article).

An improved synthesis was later developed to produce pure polycrystalline samples of $Na_3W_{1-x}Mo_xO_4F$ (x=0, 0.25, 0.5, 0.75, 1) below the melt temperature. These samples were prepared at 635 °C in air using a ramp rate of 1 °C min^{-1} and a dwell time of 20 h after reaching reaction temperature, and subsequently cooled to room temperature at 1 °C min^{-1}.

Laboratory-based X-ray powder diffraction was collected using a Rigaku Miniflex with Cu Kα radiation, and high-angle data was collected for $Na_3W_{1-x}Mo_xO_4F$ ($x=0$, 0.25, 0.5, 0.75, 1) in the range $2\theta=20$–149° on this machine.

Neutron powder diffraction (NPD) data were collected for Na_3MoO_4F and $Na_3W_{0.5}Mo_{0.5}O_4F$ at the OPAL research reactor at the Australian Nuclear Science and Technology Organisation (ANSTO). These data were collected using the high-resolution diffractometer Echidna which provides a single wavelength highly-collimated neutron beam. For this experiment, a Ge 335 monochromator was used to select a neutron wavelength $\lambda=1.6215$ Å.

Single crystals of Na_3MoO_4F were produced from $Na_2MoO_4\cdot 2H_2O$ and NaF which were ground intimately and heated at a ramp rate of 1 °C min^{-1} to 700 °C, held at 700 °C for 20 h, then cooled to room temperature at 1 °C min^{-1}. A melt was formed from which small single crystals were extracted.

A single crystal measuring 0.08 mm × 0.05 mm × 0.03 mm was selected for single crystal X-ray diffraction studies. A Bruker APEX-

II CCD diffractometer was used to collect these data using Mo Kα radiation (λ=0.71073 Å).

Selected area electron diffraction (SAED) was performed using a JEOL JEM 2100F high resolution transmission electron microscope (HRTEM).

Excitation–emission data were collected using a Perkin-Elmer LS55 spectrofluorometer with a fiber optic attachment for analyzing solid state samples.

3. Results and discussion

3.1. Power X-ray diffraction

Powder XRD data were collected in the range 2θ=120–149° for the series $Na_3W_{1-x}Mo_xO_4F$ (x=0, 0.25, 0.5, 0.75, 1) synthesized *via* incongruent melting. The lattice parameters were derived from LeBail full profile refinements carried out using the GSAS suite of programs [23]. High angle data was used in order to maximize accuracy of lattice parameter determination and to enable rapid data collection before sample degradation.

The substitution of Mo^{6+} for W^{6+} resulted in a linear contraction of the a, b, and c lattice parameters; from a=5.60518(13) Å, b=7.54686(22) Å, and c=12.9116(4) Å for Na_3WO_4F to a=5.59895(13) Å, b=7.52422(20) Å, and c=12.89340(33) Å for Na_3MoO_4F (Fig. 2a–c, Table 1). This corresponds to small decreases of the a and c parameters by 0.11% and 0.14% respectively, accompanied by a slightly larger contraction in b of 0.30%. The ionic radius of W^{6+} in tetrahedral coordination is r=0.42 Å whilst for Mo^{6+} this figure is r=0.41 Å [24] which corroborates these small contractions in lattice parameters. Considering the structure is built of face-sharing FNa_6 octahedra, it follows that the unit cell size would not change much with substitution of the smaller Mo^{6+} cation in the MO_4 units. Furthermore, the small ionic radii differences between W^{6+} and Mo^{6+} allows isovalent substitutions over the whole range of x.

Although no mention of any metastability or hygroscopic behavior was made in the previous literature which have reported the synthesis of single crystals, we observed that polycrystalline samples of Na_3MO_4F (M=Mo, W) produced from incongruent melts are at best metastable in air at room temperature. This phenomenon is most noticeable for Na_3WO_4F whereby powder XRD patterns measured over short periods of time directly after synthesis show the formation of the target phase; however, upon collecting data over a longer period of time to minimize noise ($\approx$8 h), the resultant XRD pattern contained only peaks corresponding to the cubic spinel phase Na_2WO_4 pointing to a decomposition.

To study the rate at which this decomposition in air occurs, powder XRD data was collected at 10 min intervals over the course of 2 h. These data show that the (111) and (102) peaks at $2\theta \approx 21.0°$ for Na_3WO_4F decrease in intensity over time, accompanied by the evolution of the (103), (022), and (004) peaks into a single peak at $2\theta \approx 27.6°$ which corresponds to the (220) peak of the cubic spinel phase Na_2WO_4 (Fig. 3a and b). This confirms that Na_3WO_4F decomposes rapidly to form cubic spinel-type Na_2WO_4 when exposed to air and standard laboratory humidity at room temperature (Fig. 4a).

Table 1
Lattice parameters for $Na_3W_{1-x}Mo_xO_4F$ based upon Rietveld refinement of high angle powder XRD data.

Composition	*a* (Å)	*b* (Å)	*c* (Å)
Na_3WO_4F	5.60518(13)	7.5469(2)	12.9116(4)
$Na_3W_{0.75}Mo_{0.25}O_4F$	5.60244(12)	7.53966(19)	12.9059(4)
$Na_3W_{0.5}Mo_{0.5}O_4F$	5.60202(14)	7.5347(2)	12.9018(4)
$Na_3W_{0.25}Mo_{0.75}O_4F$	5.60024(14)	7.5292(3)	12.8970(4)
Na_3MoO_4F	5.59895(13)	7.5242(2)	12.8934(3)

Interestingly, NaF is not discernible in the XRD of decomposed samples, yet upon reheating, the Na_3WO_4F phase is regenerated; thus we proposed (and later confirmed) that NaF is present in the decomposed samples in an amorphous form, possibly due to its small average particle size. XRD studies suggest that the presence of molybdenum slows the rate of decomposition. It is noticeable that the molybdenum analog, Na_3MoO_4F, is more stable and decomposes at a significantly slower rate to form Na_2MoO_4 (Fig. 4b).

The stabilization effect of incorporating molybdenum can be demonstrated by considering the area of Gaussian fit under the (111)/(102) peak for $Na_3W_{1-x}Mo_xO_4F$ (x=0, 0.5, 1) (Fig. 4c). For Na_3WO_4F, this drops off rapidly as a function of time, whereas for the Mo-containing phases Na_3MoO_4F and $Na_3W_{0.5}Mo_{0.5}O_4F$ the area under this peak decreases very slowly. It is worth noting that the partial substitution of Mo for W yields a similar effect to the 100% Mo analog, which corroborated the observation that even small amounts of Mo have a stabilizing effect.

The mixed phase $Na_3W_{0.5}Mo_{0.5}O_4F$ forms $Na_2(W, Mo)O_4$ at a similar rate to the pure-Mo phase. Smaller Mo-concentrations in the series $Na_3W_{1-x}Mo_xO_4F$ (M=Mo, W; x=0, 0.05, 0.1, 0.15, 0.2, 0.25, 0.5, 0.75, 1) were synthesized in order to determine the extent to which Mo-concentration influenced stability, and it was observed that even small concentrations of Mo down to x=0.05 significantly decreased the rate of decomposition.

It is vital to understand the decomposition at room temperature of the $Na_3W_{1-x}Mo_xO_4F$ phases formed *via* incongruent melting in order to optimize this material for use as a phosphor and/or scintillator. In addition, the spontaneous change under ambient conditions from an orthorhombic structure containing

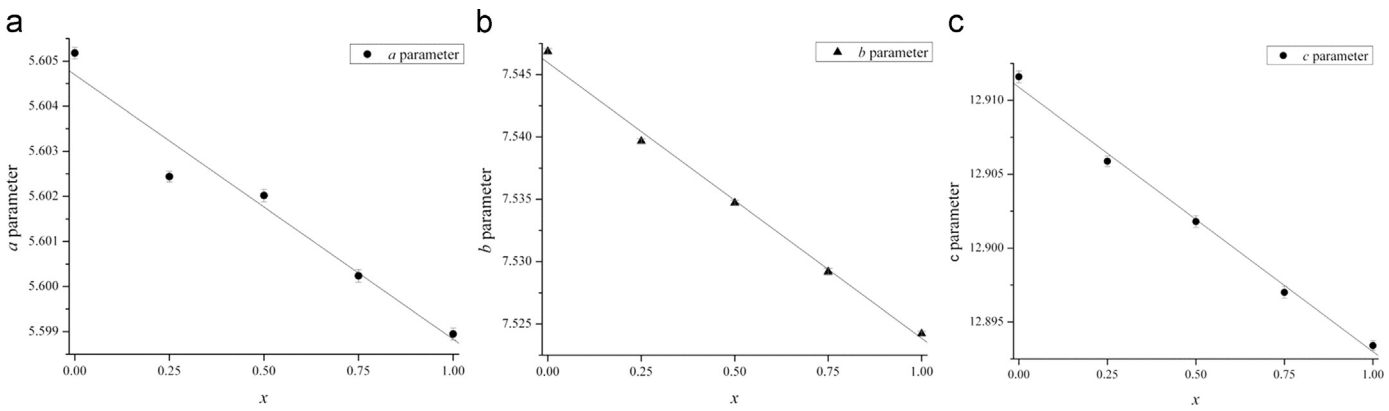

Fig. 2. $Na_3W_{1-x}Mo_xO_4F$ (x=0, 0.25, 0.5, 0.75, 1) lattice parameters trends for the (a) a parameter, (b) b parameter, and (c) c parameter.

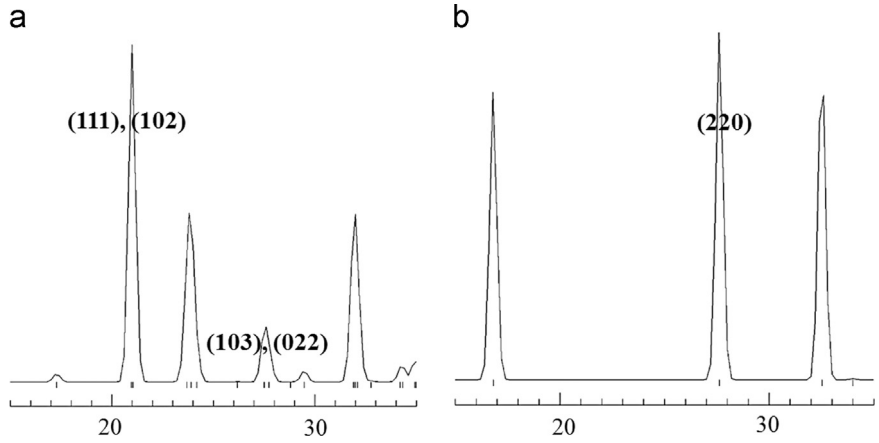

Fig. 3. Comparison of calculated XRD patterns of (a) Na_3WO_4F and (b) spinel-type Na_2WO_4. The decrease in intensity of (111) and (102) peaks at $2\theta \approx 21.0°$ for Na_3WO_4F in (a) is accompanied by the evolution of the Na_3WO_4F (103) and (022) peaks into single peak at $2\theta \approx 27.6°$ in (b) corresponding to the Na_2WO_4 (220) peak.

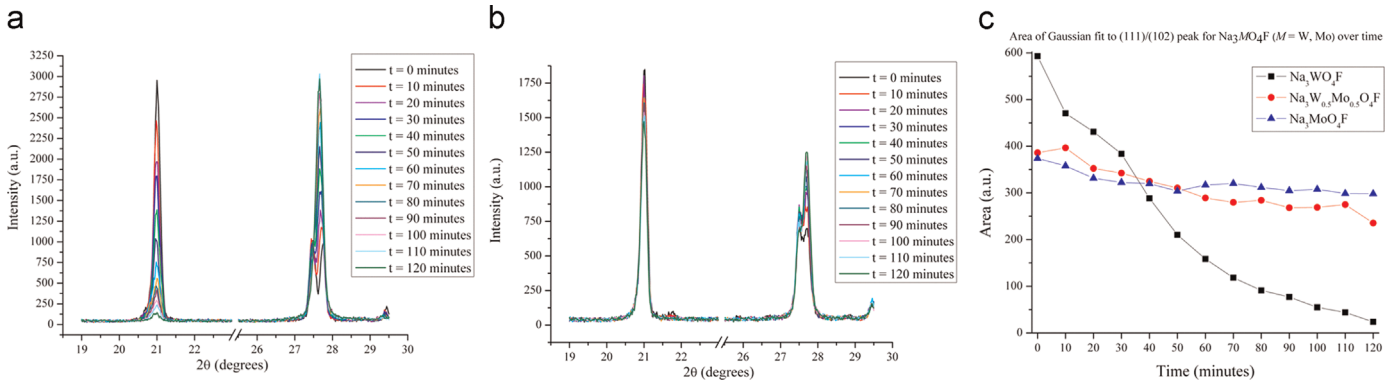

Fig. 4. Powder XRD decomposition over time of (a) Na_3WO_4F and (b) Na_3MoO_4F. The area of Gaussian fit to the (111)/(102) peak for $Na_3W_{1-x}Mo_xO_4F$ ($x=0$, 0.5, 1) as a function of time is shown in (c).

chains of face-sharing FNa_6 octahedra to a cubic spinel structure is a highly intriguing phase transition which certainly warrants further investigation.

3.2. Selected area electron diffraction

As the molybdenum analog was shown by XRD to be quantifiably more stable in air than the tungsten-containing phase, a sample of Na_3MoO_4F was examined using selected area electron diffraction (SAED) in an attempt to elucidate the decomposition mechanism to Na_2MoO_4 and NaF. The SAED patterns showed that in addition to Na_3MoO_4F (Fig. 5a), the sample contained portions of amorphous NaF (Fig. 5b) and what appears to be an incommensurate superstructure of a not yet identified sodium molybdenum oxyfluoride phase (Fig. 5c) which were not apparent in the XRD data.

We suggest that this may be a phase formed either due to not tempering the sample long enough, or inadvertently being quenched when removed from the furnace. Thus, additional samples were prepared using longer tempering times and slow-cooling at 1 °C min^{-1}. Subsequent examination using SAED confirmed that indeed the longer tempering times eliminated both the unidentified incommensurate phase and the amorphous NaF. XRD measurements monitoring the decomposition were repeated to see if the presence of the impurity phases had accelerated the decomposition to Na_2MO_4 (M=Mo, W). However, the longer tempering time and slow-cooling did not significantly improve the air/moisture stability of Na_3MO_4F (M=Mo, W).

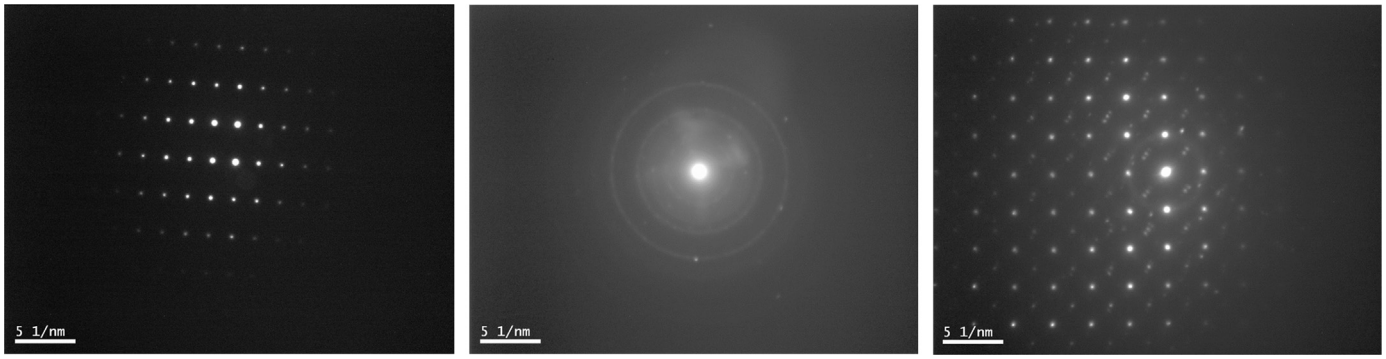

Fig. 5. TEM images (a) Na_3MoO_4F, (b) NaF, and (c) unidentified incommensurate phase.

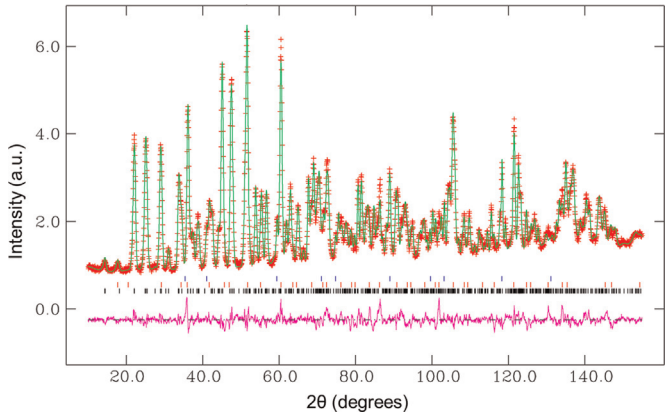

Fig. 6. Observed (red+), calculated (green) and difference (pink) profiles for $Na_3W_{0.5}Mo_{0.5}O_4F$ as generated by Rietveld profile refinement based upon NPD data with peak positions indicated by black vertical lines ($Na_2(W, Mo)O_4$ and NaF impurity peak positions marked by red and blue vertical lines respectively). (For interpretation of the references to color in this figure legend, the reader is referred to the web version of this article).

3.3. Neutron powder diffraction

In order to characterize the structures of the polycrystalline materials and ascertain the effect of *M* cation substitution, NPD data was collected on $Na_3Mo_{0.5}W_{0.5}O_4F$ and Na_3MoO_4F. Despite the selection of the more stable $x=0.5$ and $x=1$ molybdenum-containing phases and taking precautions to seal the samples in the vanadium sample can with indium wire under Ar(*g*), $Na_2(W, Mo)O_4$ and NaF impurities were present. Therefore a 3-phase Rietveld refinement was required to fit the experimental data (Figs. 6 and 7).

Obtaining a good Rietveld refinement based upon this data proved difficult due to the high amount of pseudosymmetry present; the *a* parameter of Na_2WO_4/Na_2MoO_4 (9.133(3) Å [25]/ 9.108 Å [26]) is approximately double that of NaF (4.63329(12) Å [27]). Additionally, some preferred orientation was present which was corrected for by using a spherical harmonic preferred orientation correction in the least squares fitting refinement program GSAS [23].

Rietveld refinement based upon neutron powder diffraction showed that the lattice parameters for $Na_3Mo_{0.5}W_{0.5}O_4F$ ($a=5.5930(2)$ Å, $b=7.5158(3)$ Å, $c=12.8777(4)$ Å) and Na_3FMoO_4 ($a=5.5985(2)$ Å, $b=7.5309(2)$ Å, $c=12.8936(4)$ Å) are similar to those reported from single crystal data collected for Na_3WO_4F ($a=5.5959(5)$ Å, $b=7.5102(7)$ Å, $c=12.8598(9)$ Å [17]). Refined lattice parameters and atomic positions for $Na_3Mo_{0.5}W_{0.5}O_4F$ and Na_3MoO_4F are provided in Tables 2 and 3. Selected bond lengths are listed in Table 4.

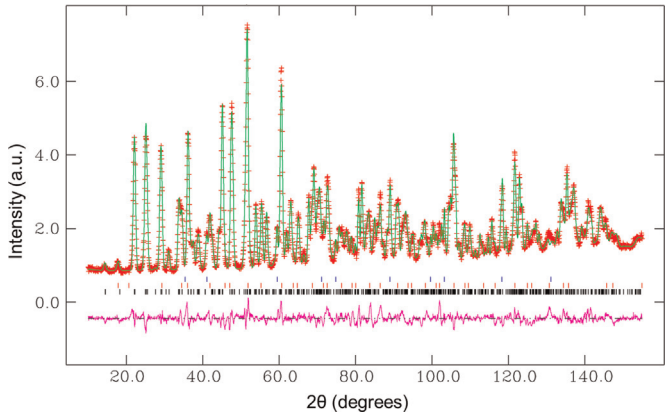

Fig. 7. Observed (red+), calculated (green) and difference (pink) profiles for Na_3MoO_4F as generated by Rietveld profile refinement based upon NPD data with peak positions indicated by black vertical lines (Na_2MoO_4 and NaF impurity peak positions marked by red and blue vertical lines respectively). (For interpretation of the references to color in this figure legend, the reader is referred to the web version of this article).

Table 2
Refined lattice parameters and atomic positions for $Na_3W_{0.5}Mo_{0.5}O_4F$ based upon NPD data.

Atom	Wyckoff position	*x*	*y*	*z*	$U_{iso} \times 100$
Na(1)	4c	0.223(1)	0.25	0.8921(5)	2.26(9)
Na(2)	8d	0.2297(9)	0.5418(6)	0.1810(4)	2.26(9)
F	4c	0.0042(8)	0.25	0.7332(3)	1.66(8)
W/Mo	4c	0.2106(7)	0.25	0.4139(3)	1.01(8)
O(1)	4c	0.3904(7)	0.25	0.0785(5)	2.83(5)
O(2)	4c	0.326(1)	0.25	0.5443(4)	2.83(5)
O(3)	8d	0.3097(6)	0.0594(4)	0.3491(3)	2.83(5)

Crystallographic data: Space group=*Pnma*, $a=5.5985(2)$ Å, $b=7.5309(2)$ Å, $c=12.8936(4)$ Å. $\chi^2=4.210$, $R_{wp}=0.0453$, $R_p=0.0351$, $R_f^2=0.0620$.

Table 3
Refined lattice parameters and atomic positions for Na_3MoO_4F based upon NPD data.

Atom	Wyckoff position	*x*	*y*	*z*	$U_{iso} \times 100$
Na(1)	4c	0.219(2)	0.25	0.8936(5)	1.81(9)
Na(2)	8d	0.230(1)	0.5413(7)	0.1803(4)	1.81(9)
F	4c	0.0064(9)	0.25	0.7326(3)	1.64(9)
Mo	4c	0.2107(7)	0.25	0.4145(3)	1.02(8)
O(1)	4c	0.3927(8)	0.25	0.0781(5)	2.74(6)
O(2)	4c	0.323(1)	0.25	0.5447(4)	2.74(6)
O(3)	8d	0.3105(8)	0.0604(4)	0.3496(3)	2.74(6)

Crystallographic data: Space group=*Pnma*, $a=5.5930(2)$ Å, $b=7.5158(3)$ Å, $c=12.8777(4)$ Å. $\chi^2=5.375$, $R_{wp}=0.0506$, $R_p=0.0400$, $R_f^2=0.0694$.

It is difficult to make a meaningful comparison between Hartenbach and Schleid's single crystal XRD data for Na_3WO_4F and the neutron powder diffraction data for $Na_3Mo_{0.5}W_{0.5}O_4F$ and Na_3MoO_4F presented herein as there are many variables in data collection and refinement strategy which lead to different systematic errors [28]. However, as the neutron powder diffraction data for the Mo-containing and mixed W/Mo materials were collected using the same instrument configuration, these data may be compared with more confidence.

The lattice parameters obtained *via* Rietveld refinement based on NPD data showed a slight contraction in lattice parameters between $Na_3Mo_{0.5}W_{0.5}O_4F$ and Na_3MoO_4F. These closely mirrored the small reduction in lattice parameters with increasing Mo-substitution observed in the laboratory-based powder XRD data,

Table 4
Selected refined bond lengths for $Na_3W_{0.5}Mo_{0.5}O_4F$ and Na_3MoO_4F from Rietveld refinement based on NPD data.

Bond	$Na_3W_{0.5}Mo_{0.5}O_4F$ Length (Å)	Na_3MoO_4F Length (Å)
Na(1)–O(1)	2.580(9)	2.566(9)
Na(1)–O(2)	2.368(9)	2.36(1)
Na(1)–O(3)	2.402(4) [× 2]	2.406(4) [× 2]
Na(1)–F	2.386(8), 2.257(8)	2.391(9), 2.284(9)
Na(2)–O(1)	2.718(5)	2.712(5)
Na(2)–O(2)	2.379(6)	2.366(6)
Na(2)–O(3)	2.340(6)	2.353(6)
Na(2)–O(3′)	2.502(7)	2.497(8)
Na(2)–F	2.265(6)	2.256(7)
Na(2)–F′	2.323(6)	2.497(8)
W/Mo–O(1)	1.795(6)	1.781(6)
W/Mo–O(2)	1.801(6)	1.791(6)
W/Mo–O(3)	1.752(3) [2]	1.744(3) [× 2]

with a 0.12% decrease in both the a and c parameters and a slightly larger contraction in b of 0.20%.

Closer analyses of these data applying the bond valence model were performed. The experimental bond valence (S) is calculated from the observed bond length (r) using Eq. (1):

$$S = \exp\left[(r_0 - r)/B\right] \quad (1)$$

where r_0 is the notional length of a bond of unit valence, many of which have been tabulated [29,30] and B is the softness parameter, for which a value of 0.37 Å is generally assumed.

When the crystallographic structure is known, the experimental bond valences around a given ion can be summed to give the bond valence sum, $\Sigma_j S_{ij}$. The strain experienced by an individual ion, i, is expressed by the difference of the bond valence sum, S_{ij}, around ion i and its anticipated atomic valence, V_i. This difference is known as the discrepancy factor, d_i, and may be expressed mathematically as shown in Eq. (2) [31,32]:

$$d_i = \sum_j S_{ij} - V_i \quad (2)$$

The sign of d_i is indicative of the nature of the strain present about ion i: if the value of d_i is positive then the bonds are compressed whereas if d_i is negative they are elongated. The global instability index (G) is calculated using Eq. (3) and is simply the average over the N atoms in the formula unit of the root-mean-square deviation of the discrepancy factors from the anticipated atomic valence (V_i):

$$G = \left(\sum_i \{d_i\}^2/N\right)^{\frac{1}{2}} \quad (3)$$

The global instability index can be used to quantify the degree of strain present in a crystal structure. The units of G are vu (valence unit). Typically, a structure with $G < 0.1$ is categorized as stable whereas structures with $0.1 \leq G \leq 0.2$ experience strain. It is unusual for a structure to have $G > 0.2$ and such a result may indicate a structural model is not correct [31–33].

Global instability factors based on bond valence sums calculated from the bond distances obtained by Rietveld refinement of the NPD data are shown in Table 5.

The global instability factor for both $Na_3Mo_{0.5}W_{0.5}O_4F$ and Na_3MoO_4F was 0.15 vu which falls into the range categorized as indicative for the presence of strain (0.1–0.2 vu [32,33]). This is in line with the observation that polycrystalline samples of $Na_3W_{1-x}Mo_xO_4F$ consistently decomposed to spinel Na_2WO_4/Na_2MoO_4 and NaF during the course of this study. It is well established that face-sharing octahedra are more prone to developing strain as a result of size variations introduced by substitutions than edge- or corner-sharing ones. It is also likely that repulsions between F^- anions in the adjacent face-sharing FNa_6 octahedra drive the decomposition to the spinel phase. The identical G values calculated for $Na_3Mo_{0.5}W_{0.5}O_4F$ and Na_3MoO_4F support the observation shown in Fig. 4c that partial substitution of Mo^{6+} for W^{6+} is just as effective in stabilizing polycrystalline samples against decomposition as complete Mo^{6+} substitution.

Table 5
Summary of atomic valence (V_i), bond valence sums calculated using weighted r_0 values based upon fractional site occupancies (S_{ij}) and discrepancy factors (d_i) in order to calculate global instability index (G) for $Na_3W_{0.5}Mo_{0.5}O_4F$ and Na_3MoO_4F based on NPD data.

Atom	V_i	$Na_3W_{0.5}Mo_{0.5}O_4F$		Na_3MoO_4F	
		S_{ij}	d_i	S_{ij}	d_i
Na(1)	1	1.092	0.092	1.080	0.080
Na(2)	1	1.059	0.059	1.002	0.002
F	1	1.113	0.113	0.975	−0.025
W/Mo	6	5.804	−0.196	5.881	−0.119
O(1)	2	1.663	−0.337	1.704	−0.296
O(2)	2	1.989	−0.011	1.809	−0.191
O(3)	2	2.125	0.125	2.219	0.219
G		0.15		0.15	

Table 6
Refined lattice parameters and atomic positions for Na_3MoO_4F based on single crystal XRD data.

Atom	Wyckoff position	x	y	z	$U_{iso} \times 100$
Na(1)	4c	0.2275(2)	0.25	0.89260(9)	1.71(2)
Na(2)	8d	0.23043(13)	0.53971(11)	0.17940(6)	1.689(17)
F	4c	0.0022(3)	0.25	0.73279(12)	1.50(3)
Mo	4c	0.20896(4)	0.25	0.41606(2)	1.043(8)
O(1)	4c	0.3944(4)	0.25	0.07917(18)	3.49(6)
O(2)	4c	0.3233(4)	0.25	0.54296(15)	1.95(4)
O(3)	8d	0.3095(3)	0.0597(2)	0.35005(11)	2.47(3)

Crystallographic data: Space group=*Pnma*, lattice parameters a=5.5936(2) Å, b=7.5118(2) Å, c=12.8826(4) Å, V=541.30(3) Å^3, Z=4.

3.4. Single crystal X-ray diffraction

In order to overcome the stability issues of polycrystalline samples of $Na_3W_{1-x}Mo_xO_4F$ and to make a valid comparison with the single crystal data for Na_3WO_4F presented by Hartenbach and Schleid, X-ray diffraction data were collected on a Na_3MoO_4F single crystal. These data confirmed the space group assignment of *Pnma* and determined the lattice parameters for Na_3MoO_4F to be a=5.5936(2) Å, b=7.5118(2) Å, and c=12.8826(4) Å. Atomic positions and selected bond lengths for a single crystal of Na_3MoO_4F are presented in Tables 6 and 7 respectively.

In order to ascertain whether the metastability observed in polycrystalline samples is derived from strain within the crystal lattice, the bond lengths for Na_3WO_4F reported by Hartenbach and Schleid [17] from single crystal data were used as a basis for bond valence sum and global instability index calculations. These are summarized in Table 8. The global instability factor calculated from these data was 0.09 vu, which is at the borderline between a strained and unstrained structure ($G < 0.1$ vu) [32,33]. As the evidence for strain was less clear-cut from the single crystal data for Na_3WO_4F than the NPD data for $Na_3Mo_{0.5}W_{0.5}O_4F$ and Na_3MoO_4F, this raised the question of whether strain only arose from the incorporation of Mo^{6+} on the W^{6+} or whether the strain was indeed present in all $Na_3W_{1-x}Mo_xO_4F$ (x=0, 0.25, 0.5, 0.75, 1) materials and only elucidated by the superior unit cell parameters and atom positions obtained from powder diffraction studies.

Table 7
Selected refined bond lengths for Na_3MoO_4F from single crystal XRD data.

Bond	Length (Å)
Na(1)–O(1)	2.408(2)
Na(1)–O(2)	2.579(3)
Na(1)–O(3)	2.3993(15) [× 2]
Na(1)–F	2.2296(18), 2.4138(18)
Na(2)–O(1)	2.6919(16)
Na(2)–O(2)	2.3823(16)
Na(2)–O(3)	2.3636(16)
Na(2)–O(3′)	2.4990(17)
Na(2)–F	2.2814(13)
Na(2)–F′	2.3385(13)
Mo–O(1)	1.760(2)
Mo–O(2)	1.7556(19)
Mo–O(3)	1.7557(15) [× 2]

Table 8
Summary of atomic valence (V_i), bond valence sums (S_{ij}) and discrepancy factors (d_i) in order to calculate global instability index (G) for Na_3WO_4F and Na_3MoO_4F. Based upon single crystal XRD data for Na_3WO_4F published by Hartenbach and Schleid [17] and single crystal XRD data for Na_3MoO_4F reported herein.

Atom	V_i	Na_3WO_4F		Na_3MoO_4F	
		S_{ij}	d_i	S_{ij}	d_i
Na(1)	1	1.099	0.099	1.078	0.078
Na(2)	1	1.055	0.055	1.034	0.034
F	1	1.064	0.064	1.086	0.086
W/Mo	6	5.944	−0.056	6.004	0.004
O(1)	2	1.826	−0.174	1.864	−0.136
O(2)	2	2.136	0.136	2.046	0.046
O(3)	2	2.063	0.063	2.077	0.077
G		0.09		0.07	

Refined bond lengths for Na_3MoO_4F based upon single crystal XRD data were used to calculate bond valence sums (S_{ij}) and the global instability index (G). These results are tabulated alongside those for Na_3WO_4F in Table 8. The global instability index was $G=0.07$ for a single crystal of Na_3MoO_4F, which is slightly less than that calculated from Hartenbach and Schleid's data for Na_3WO_4F ($G=0.09$). The bond valence sum for W and ($S_{ij}=5.94$) and Mo ($S_{ij}=6.00$) reveal that both metals are close to their formal valence.

Comparison of the discrepancy factors d_i (which are a measure of the strain experienced by an individual ion) between the single crystal and powder data may yield some clues as to why the polycrystalline samples prepared from incongruous melting were metastable in air. The d_i values for the O atoms in the polycrystalline sample Na_3MoO_4F ($d_i=-0.296$, -0.191, 0.219) are slightly larger than those reported for the single crystal of Na_3MoO_4F ($d_i=-0.136$, 0.046, 0.077), suggesting that the MoO_4 tetrahedra might be slightly more strained in the polycrystalline sample produced from incongruent melting than in the single crystal. It is likely that this observed strain is still present in single crystals of this material, but the accuracy of atomic positions in the single crystal data does not give as clear an indication of this as powder data.

As G based on single crystal data was similar for both Na_3WO_4F (0.09) and Na_3MoO_4F (0.07) and G based on NPD data was 0.15 for both $Na_3W_{0.5}Mo_{0.5}O_4F$ and Na_3MoO_4F, the evidence suggests that the strain present in the overall structure is not appreciably altered by the substitution of Mo^{6+} for W^{6+}.

3.5. Photoluminescence

In order to collect photoluminescent data, pure polycrystalline samples which did not decompose to form Na_2WO_4/Na_2MoO_4 and NaF were required. An improved synthesis method below the melting point was used to produce stable polycrystalline samples. Powder X-ray diffraction showed that synthesis at 635 °C yielded polycrystalline samples of $Na_3W_{1-x}Mo_xO_4F$ ($x=0$, 0.25, 0.5, 0.75, 1) that were stable in air at room temperature.

Excitation–emission spectra for the series $Na_3W_{1-x}Mo_xO_4F$ ($x=0$, 0.25, 0.5, 0.75, 1) are shown in Fig. 8. Upon excitation with $\lambda=254$ nm and $\lambda=365$ nm, all samples exhibited a self-activating broad emission centered at $\lambda\approx485$ nm. The excitation spectra show broad excitations in the ranges 230–270 nm (taking the form of a single broad peak in this region for Na_3WO_4F and two peaks centered at 236 nm and 256 nm for the Mo-containing phases) and 320–380 nm. Both of the regions would be amenable to excitation by $\lambda=254$ nm and $\lambda=365$ nm in a compact fluorescent light. The breadth of the second excitation region 320–380 nm in the near-UV region of the spectrum is close to the emission from pure GaN LEDs (370 nm) thus the $Na_3W_{1-x}Mo_xO_4F$ ($x=0$, 0.25, 0.5, 0.75, 1) family may provide novel host lattices for new PC-LED phosphors.

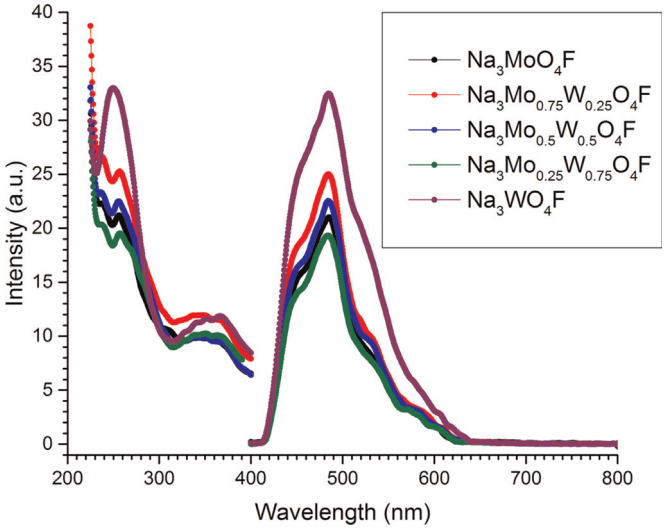

Fig. 8. Excitation–emission spectra for $Na_3W_{1-x}Mo_xO_4F$ ($x=0$, 0.25, 0.5, 0.75, 1).

Table 9
Summary of excitation and emission maxima and corresponding CIE coordinates for the series $Na_3W_{1-x}Mo_xO_4F$ ($x=0$, 0.25, 0.5, 0.75, 1).

Composition	λ_{ex} (nm)	λ_{em} (nm)	CIE coordinates	
			x	***y***
Na_3MoO_4F	256	485	0.1711	0.2437
$Na_3Mo_{0.25}W_{0.75}O_4F$	257	485	0.1727	0.2433
$Na_3Mo_{0.5}W_{0.5}O_4F$	256	485	0.1733	0.2502
$Na_3Mo_{0.25}W_{0.75}O_4F$	257	485	0.1731	0.2476
Na_3WO_4F	250	485	0.1807	0.2796

The CIE coordinates calculated from the emission spectra are shown in Table 9 and are plotted in Fig. 10 for the end members of the family, Na_3MoO_4F and Na_3WO_4F. The slight difference between the Mo and W phases shows that some small degree of tuning could be performed on a phosphor by choosing the appropriate host lattice. The emission spectra, although peaking at $\lambda\approx485$ nm in the blue part of the visible spectrum, is very broad, ranging from $\lambda\approx420$ nm to $\lambda\approx630$ nm. This suggests that incorporating dopant amounts of red emitters into these materials could be used to coax the overall phosphor output towards the white region. The tungsten end-member of the family Na_3WO_4F displays slightly higher intensity excitation and emissions, so may be a better choice to optimize new phosphors based on these materials.

A preliminary experiment was carried out to determine whether rare earth cations could be incorporated into this new family of host lattices. The Eu^{3+}-doped samples $Na_{2.85}Eu_{0.05}MoO_4F$ and $Na_{2.85}Eu_{0.05}WO_4F$ were prepared *via* incongruent melts. Excitation–emission spectra for these materials are shown in Fig. 9 with the corresponding CIE coordinates plotted in Fig. 10. These spectra displayed the characteristic line emissions associated with Eu^{3+} whilst retaining the broad self-activated photoluminescence from the host lattice.

Excitation of $Na_{2.85}Eu_{0.05}WO_4F$ with $\lambda=391$ nm yielded an emission with CIE coordinates $x=0.3188$, $y=0.2859$, whilst the emission exhibited by $Na_{2.85}Eu_{0.05}MoO_4F$ upon excitation by $\lambda=289$ nm gave $x=0.39060$, $y=0.3181$. Both of these overall emissions are closer to the white region on the CIE diagram, suggesting that careful optimization of dopants and W/Mo composition could produce a phosphor with overall white light output.

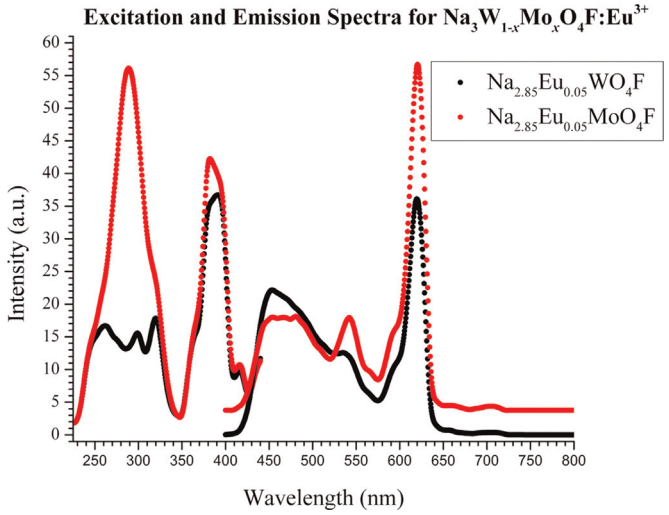

Fig. 9. Excitation–emission spectra for $Na_{2.85}Eu_{0.05}WO_4F$ and $Na_{2.85}Eu_{0.05}MoO_4F$.

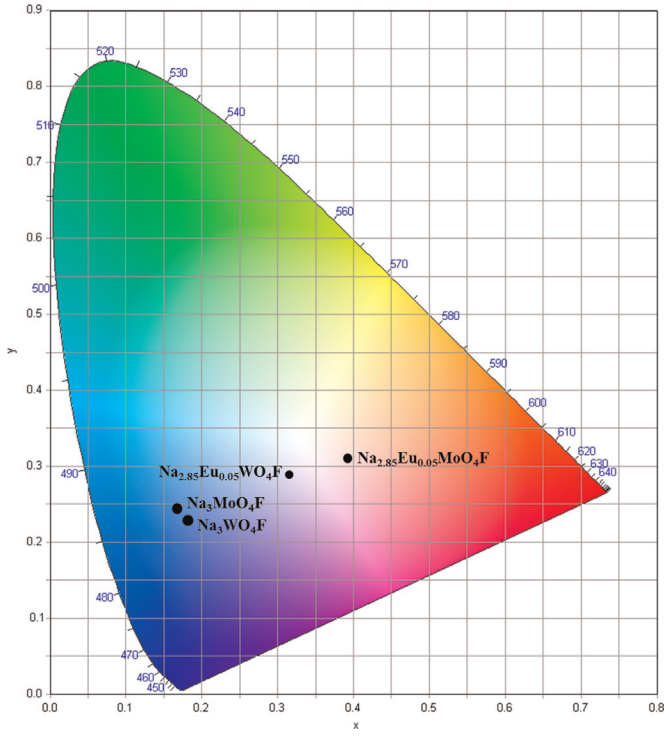

Fig. 10. CIE coordinates for Na_3MoO_4F and Na_3WO_4F (λ_{ex}=256 nm), $Na_{2.85}Eu_{0.05}WO_4F$ (λ_{ex}=391 nm) and $Na_{2.85}Eu_{0.05}MoO_4F$ (λ_{ex}=289 nm).

4. Conclusions

This work has established the first directed synthesis of the ordered oxyfluorides $Na_3W_{1-x}Mo_xO_4F$ ($0 \le x \le 1$) and provides the first example of photoluminescence in these materials. The molybdenum analog, Na_3MoO_4F, of the known oxyfluoride Na_3WO_4F has been synthesized for the first time and has been shown *via* neutron powder and single crystal diffraction studies to be isostructural with the tungsten species. Phases produced from incongruent melts are metastable with SAED pointing to the presence of incommensurate super structures depending on the synthesis conditions. The addition of even small amounts of molybdenum has been shown to stabilize mixed phases, although this was not reflected in calculations of global instability index which did not vary with substitution of Mo^{6+} for W^{6+} in polycrystalline samples. An improved low temperature synthesis route allows for facile one-step synthesis of polycrystalline members of the $Na_3W_{1-x}Mo_xO_4F$ family from $Na_2WO_4 \cdot 2H_2O$, $Na_2MoO_4 \cdot H_2O$, and NaF with improved stability. A complete solid solution $Na_3W_{1-x}Mo_xO_4F$ ($0 \le x \le 1$) is available and self-activating photoluminescence has been investigated for x=0, 0.25, 0.5, 0.75, 1. $Na_3W_{1-x}Mo_xO_4F$ materials have a broad absorption in the near-UV region which is close to the emission from pure GaN LEDs (370 nm) thus may provide promising new host lattices for new PC-LED phosphors. Doping with Eu^{3+} has been shown to shift the overall photoluminescent output of these materials closer to the Planckian locus, demonstrating the potential of these materials as suitable host lattices for rare earth emitters. Coupled with the differences in self-activating photoluminescence between Mo- and W-containing species yielding a significant difference in emission output of the Eu^{3+}-doped phases, the $Na_3W_{1-x}Mo_xO_4F$ host lattice provides the potential to tailor photoluminescent behavior to design novel phosphor materials.

Acknowledgments

We would like to thank the NSF (Grant no. CHE-103689) for funding the single crystal X-ray diffractometer at Illinois State University.

References

[1] R.O. Keeling Jr., Acta Crystallogr. 10 (1957) 209–213.
[2] R.M. Hazen, L.W. Finger, J.W.E. Mariathasan, J. Phys. Chem. Solids 46 (2) (1985) 253–263.
[3] M.J. Treadway, R.C. Powell, J. Chem. Phys. 61 (10) (1974) 4003–4011.
[4] M.V. Nazarov, D.Y. Jeon, J.H. Kang, E.-J. Popovici, L.-E. Muresan, M. V. Zamoryanskaya, B.S. Tsukerblat, Solid State Commun. 131 (2004) 307–311.
[5] V.B. Mikhalik, H. Kraus, D. Wahl, M. Itoh, M. Koike, I.K. Bailiff, Phys. Rev. B 69 (2004) 205110.
[6] L.S. Dent Glasser, F.P. Glasser, Acta Crystallogr. 18 (1965) 453–454.
[7] V.B. Mikhalik, H. Kraus, G. Miller, M.S. Mykhaylyk, D. Wahl, J. Appl. Phys. 97 (2005) 083523.
[8] I. Földvari, Á. Péter, S. Keszthelyi-Lándori, R. Capelleti, J. Cryst. Growth 79 (1986) 714–719.
[9] S. Neeraj, N. Kijima, A.K. Cheetham, Chem. Phys. Lett. 387 (2004) 2–6.
[10] E. Sullivan, T. Vogt, ECS J. Solid State Sci. Technol. 2 (2) (2013) R3088–R3099.
[11] R. Domesle, R. Hoppe, Z. Anorg. Allg. Chem. 492 (1982) 63–68.
[12] C.C. Toradi, L.H. Brixner, Mat. Res. Bull. 20 (1985) 137–145.
[13] G. Blasse, H.C.G. Verhaar, M.J.J. Lammers, G. Wingefeld, R. Hoppe, P. de Mayer, J. Lumin. 29 (5–6) (1984) 497–499.
[14] M. Wiegel, G. Blasse, Solid State Commun. 86 (4) (1993) 239–241.
[15] V.B. Mikhalik, H. Kraus, V. Kapustyanyk, M. Panasyuk, Y. Prots, V. Tsybulskyi, L. Vasylechko, J. Phys. Condens. Matter 20 (2008) 365219.
[16] O. Schmitz-Dumont, A. Weeg., Z. Anorg. Allg. Chem. 265 (1951) 139–155.
[17] I. Hartenbach, T. Schleid, Z. Anorg. Allg. Chem. 633 (4) (2007) 524–526.
[18] Ö. Andaç, F.P. Glasser, R.A. Howie, Acta Crystallogr. C53 (1997) 831–833.
[19] L.F. Schneemeyer, L. Guterman, T. Siegrist, G.R. Kowach, J. Solid State Chem. 160 (2001) 33–38.
[20] S. Park, T. Vogt, J. Lumin. 129 (2009) 952–957.
[21] A. Akella, D.A. Keszler, Chem. Mater. 7 (1995) 1299–1302.
[22] V. Sivakumar, U.V. Varadaraju, J. Electrochem. Soc. 156 (7) (2009) J179–J184.
[23] A.C. Larson, R.B. Von Dreele, General structure analysis system (GSAS), Los Alamos National Laboratory Report LAUR 86-748 (2004).
[24] R.D. Shannon, Acta Crystallogr. A32 (1976) 751–767.
[25] K. Okada, H. Morikawa, F. Marumo, S. Iwai, Acta Crystallogr. B30 (1974) 1872–1873.
[26] PDF 00-12-0073/Natl Bur Stand.
[27] PDF 00-036-1455/McMurdie Powder Diffrac.
[28] R.J. Hill, L.M.D. Cranswick, J. Appl. Crystallogr. 27 (1994) 802–844.
[29] I.D. Brown, D. Altermatt, Acta Crystallogr. B41 (1985) 244–247.
[30] I.D. Brown, Chem. Rev. 109 (2009) 201–211.
[31] D. Altermatt, I.D. Brown, Acta Crystallogr. B41 (1985) 240–244.
[32] A. Salinas-Sanchez, J.L. Garcia-Munoz, J. Rodriguez-Carvajal, R. Saez-Puche, J. L. Martinez, J. Solid State Chem. 100 (1992) 201–211.
[33] E. Sullivan, M. Avdeev, T. Vogt, J. Solid State Chem. 194 (2012) 297–306.